



POLITECNICO
MILANO 1863

[RE.PUBLIC@POLIMI](#)

Research Publications at Politecnico di Milano

Post-Print

This is the accepted version of:

X. Wang, P. Xia, P. Masarati
Active Aeroelastic Control of Aircraft Wings with Piezo-Composite
Journal of Sound and Vibration, Vol. 455, 2019, p. 1-19
doi:10.1016/j.jsv.2019.04.035

The final publication is available at <https://doi.org/10.1016/j.jsv.2019.04.035>

Access to the published version may require subscription.

When citing this work, cite the original published paper.

Permanent link to this version

<http://hdl.handle.net/11311/1089187>

Active aeroelastic control of aircraft wings with piezo-composite

Xiao Wang, Pinqi Xia*

*National Key Laboratory of Rotorcraft Aeromechanics, College of Aerospace Engineer,
Nanjing University of Aeronautics and Astronautics, No.29 Yudao St., 210016, Nanjing,
Jiangsu Province, China.*

Pierangelo Masarati

*Dipartimento di Scienze e Tecnologie Aerospaziali, Politecnico di Milano, Via La Masa 34,
20156 Milano, Italy*

Abstract

Active control of swept smart aircraft wings in an incompressible flow are examined. The wing structure is modeled as a composite thin-walled beam featuring fiber-reinforced host structure and piezo-composite actuators. The nonclassical effects, such as twist-bending elastic coupling, warping inhibition, transverse shear and rotatory inertia are incorporated. The unsteady incompressible aerodynamics are derived based on the concept of indicial functions, applicable to arbitrary small motion in the time domain. The influence of directionality property both of the host structure and piezo-actuators on improving aeroelastic performance are specifically investigated. The potential for active aeroelastic control via the actuation couplings due to the anisotropic piezoelectric properties is highlighted. A number of conclusions are outlined at the end.

Keywords: aeroelastic control, elastic tailoring, actuation couplings, piezo-composite

*Corresponding author

Email addresses: xiao.wang@polimi.it; x.wang@nuaa.edu.cn (Xiao Wang),
xiapq@nuaa.edu.cn (Pinqi Xia), pierangelo.masarati@polimi.it (Pierangelo Masarati)

Nomenclature

a_{ij}	1-D global stiffness coefficients
\mathcal{A}_i^X	piezo-coefficients in Eq. (10)
b_{ij}	1-D global mass coefficients
$2b, 2d$	width and depth of the beam cross-section, see Fig. 1
\bar{B}_w, \tilde{B}_w	bimoment of the piezo-actuator contribution
$C_{L\phi}$	local lift curve slope
$F_w(s), a(s)$	primary and secondary warping functions
\tilde{Q}_z	flapwise transverse shear force of the piezo-actuator contributions
h	thickness of the wall
$H(\cdot)$	Heaviside step function
k_B, k_T	control gains for bending and twist control methodologies, respectively
L	length of the beam, see Fig. 1
L_C, L_{ae}, T_{ae}	circulatory lift force, aerodynamic lift and twist moment, respectively
m_h, m_p	numbers of the host structure layers and the piezo-composite layers, respectively
\tilde{M}_x	flapwise bending moment of the piezo-actuator contribution
\tilde{M}_y	torque of the piezo-actuator contribution
$R(y)$	piezo-actuator span location
(s, y, n)	local coordinates for the cross-section, see Fig. 1
u_0, v_0, w_0	displacement components of the cross-section along $x-$, $y-$, $z-$ axis, see Fig. 1
U_n, U_∞, U_g	freestream speed, speed normal to the leading edge and peak gust velocity, respectively.
V, V_T, V_B	voltages applied on the piezo-composite lamina
$V_1, V_2,$	voltage parameters in Eq. (12)
$w_{c/2}, w_{3c/4}$	the downwash quantities at the mid- and three-quarter-chord locations
Λ	sweep angle, backward positive, see Fig. 2
ρ_∞	density of the air
δ	variation operator
δ_p, δ_s	tracers that take the value 1 or 0
θ_h, θ_p	ply-angles in host structure and piezo-actuator, respectively
θ_x, ϕ, θ_z	rotations of the cross-section about $x-$, $y-$, $z-$ axis, see Fig. 1

$\dot{()}, \ddot{()}, ()'$	$\partial()/\partial t, \partial^2()/\partial t^2, \partial()/\partial y$
\mathbf{X}^T	transpose of the matrix or vector \mathbf{X}
\oint_c, \int_0^L	integral along the cross-section and the span, respectively

1. Introduction

Due to the great advantages such as light weight, high strength and design flexibility, composite thin-walled structures are expected to meet the increasingly aggressive missions of the modern high-performance aircrafts [1, 2]. These vehicles are designed to operate in severe environmental conditions, such as gust, blast, sonic-boom, shock wave, etc [3]. Working in such a harsh environment, the aircraft wing structure may experience intense oscillations leading to failure by fatigue even in the subcritical flight speed range. Thus in order to improve the level of the vehicles' operational qualities, implementation of adequate control capabilities are required.

Compared with the metallic thin-walled beams, the composite ones exhibit several noticeable non-classical effects, such as material anisotropy, elastic couplings, significant transverse shear strain and warping inhibitions (see, e.g., [4–9]). A series of investigation about the implication of these effects on the aeroelastic behavior were conducted (see, e.g., [10–17]). Although suitable elastic tailoring offers a beneficial influence on the dynamic response characteristics, this technique is passive in nature in the sense that, once implemented, the structure cannot respond to the variety of factors under which it must operate. Since piezoelectric materials have a lot desirable characteristics, such as self-sensing, structure embeddability, fast response and covering a broad range of frequency, as a complementary option, active control via the implementation of piezoelectric materials can be applied to enhance the dynamic aeroelastic response and to avoid the occurrence of the structural resonance and of any dynamic instability [18].

In the existing literature, significant work on modeling or studying active

aeroelastic control of smart aircraft wings are based on the assumption of the isotropy of piezo-actuators constituent material [19–21]. As a result, the control system can just be designed based on a piezoelectric bending moment control, lacking the piezoelectric torque control. Wang et al [22, 23] developed a composite thin-walled beam theory with anisotropy piezo-composite (e.g. MFC [24] and AFC [25]), and gave a comprehensive discussion on couplings of piezoelectric extension, transverse shear, twist, bimoment and bending actuations.

In the present article, we approach the problem in an extended context in the sense that the smart aircraft wings are modeled as anisotropic thin-walled beams with piezo-composite in incompressible flow. The implications of implementations both of the elastic tailoring of fiber-reinforced host structure and anisotropic characteristics of piezo-composite on the dynamic aeroelastic response are investigated. Special attention is given to the formulation of the problem. It is assumed that the piezo-actuators are bonded or embedded in the host structure by circumferentially asymmetric stiffness (CAS) configuration. A negative velocity feedback control methodology is implemented to alleviate the aeroelastic response and to postpone the occurrence of flutter. Relations between control authority and tailoring of piezo-actuators are investigated via studying damping ratios of the system.

2. Aeroelastic governing equations and solution methodology

2.1. Structural model

A single-cell, closed cross-section, thin-walled beam model incorporating fiber-reinforced and piezoelectric composite materials is used in the modeling of adaptive aircraft wings and toward the study of active aeroelastic control. The geometry of the wing structure and the chosen coordinate systems are indicated in Fig. 1. Toward the modeling of the wing structure, the following assumptions are adopted:

1. Since the original cross-sectional shape of aircraft wings is maintained by a system of transverse stiffening members (ribs), the beam cross-sections

are assumed rigid in their own plane, but are allowed to warp out of their original planes during the deformation.

2. Both primary and secondary warping effects are accounted. In addition, transverse shear effects are included.
3. Anisotropic piezoelectric properties of piezo-composite materials are highlighted.

Following the discussion and derivation in [26, 27], the representation of the three dimensional displacements quantities based on the hypothesis of small deflection angle is postulated:

$$u(x, y, z, t) = u_0(y, t) + z\phi(y, t), \quad (1a)$$

$$v(x, y, z, t) = v_0(y, t) + \left[x(s) - n \frac{dz}{ds} \right] \theta_z(y, t) + \left[z(s) + n \frac{dx}{ds} \right] \theta_x(y, t) - [F_w(s) + na(s)] \phi'(y, t), \quad (1b)$$

$$w(x, y, z, t) = w_0(y, t) - x\phi(y, t), \quad (1c)$$

where $F_w(s)$ and $a(s)$ are the primary and secondary warping functions, respectively (e.g. see Ref. [27]); u_0 , v_0 , w_0 are the displacement components of the cross-section along x -, y -, z -axis; while θ_x , ϕ , θ_z denote the associated rotations of the cross-section, see Fig. 1. These six kinematic variables, which represent one dimensional displacement measures, constitute the basic unknowns of the problem.

2.2. Unsteady aerodynamic loads for arbitrary small motion in incompressible flow

Based on the two-dimensional incompressible unsteady strip theory aerodynamics and the the modified strip theory for a finite-span wing is used [28, 29],

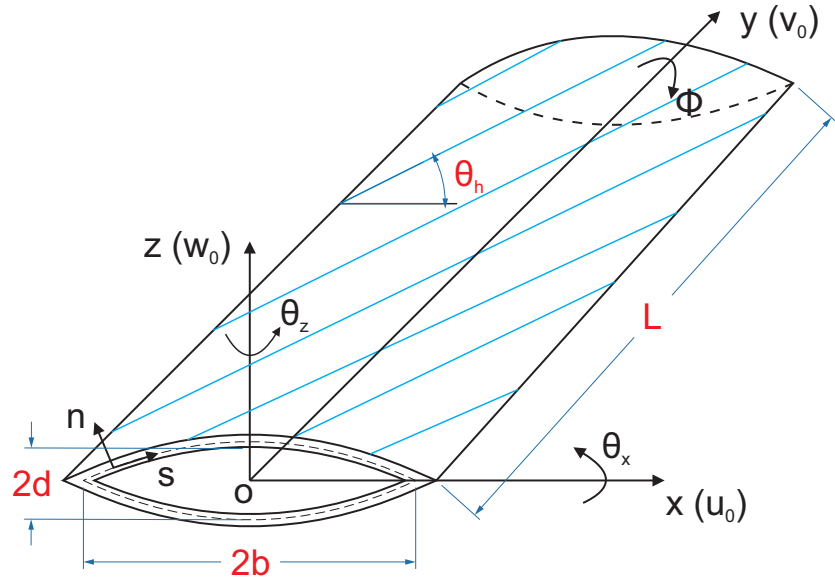


Figure 1: Geometry of an aircraft wing modeled as thin-walled beam with a biconvex cross-section (local coordinate frame (s, y, n) is on the mid-line contour of the cross-section).

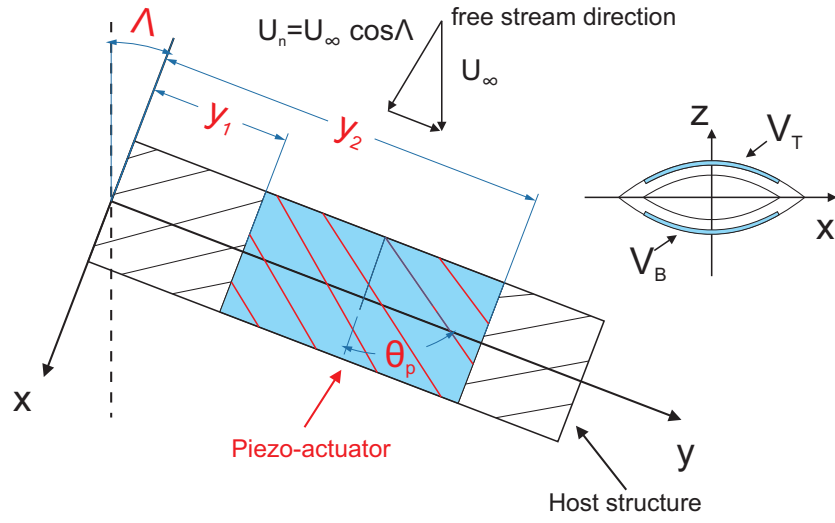


Figure 2: A smart aircraft wing with piezo-actuator.

the aerodynamic lift L_{ae} and twist moment T_{ae} about the beam coordinate system $oxyz$ in Fig. 2 can be expressed in the time domain [12]

$$L_{ae}(y, t) = \underline{-\pi\rho_\infty b^2 [\dot{w}_{c/2}(y, t)]} - L_C(y, t), \quad (2a)$$

$$T_{ae}(y, t) = \underline{-\pi\rho_\infty b^3 \left[\frac{1}{2}U_n\dot{\phi}(y, t) + \frac{1}{8}b\ddot{\phi}(y, t) \right]} - \frac{1}{2}bL_C(y, t). \quad (2b)$$

In Eqs. 2, the underscored terms are associated with non-circulatory part of aerodynamic loads (e.g., see Ref. [30]); U_n is the freestream speed normal to the leading edge (see Fig. 2); $w_{c/2}$ denotes the downwash at the middle chord points measured from the leading edge of the airfoil; ρ_∞ is density of air; L_C is the circulatory lift force which can be written as

$$L_C(y, t) = 2\pi\rho_\infty U_n b \left\{ w_{3c/4}(y, t)\phi_w \left(\frac{U_n t}{b} \right) + \int_0^t \frac{dw_{3c/4}(y, \tau)}{d\tau} \phi_w \left[\frac{U_n}{b}(t - \tau) \right] d\tau \right\}, \quad (3)$$

where ϕ_w is Wagner's function, which is related to Theodoresn's lift deficiency function through a Fourier transform; $w_{3c/4}$ denotes the downwash at the three quarters chord point. Note that, the adopted aerodynamic model, which is based on the thin-airfoil theory and small perturbation assumption, is valid for a lightly inclined, thin, uncambered airfoil, that means it is valid for the airfoil with a biconvex cross-section we investigate herein. In other words, the effects of camber and constant initial angle of attack are not included in this paper. However, these can be handled by steady-flow theory and the results afterward superimposed on what we calculated if needed.

To cast L_{ae} and T_{ae} into state space form, a general two term exponentially growing indicial function ϕ_w in Eq. (3) is assumed such that [31, p.285]

$$\phi_w(t) = 1.0 - 0.165e^{-0.0455\frac{U_n}{b}t} - 0.335e^{-0.3\frac{U_n}{b}t}. \quad (4)$$

Thus the unsteady aerodynamic lift and twist moment can be expressed in state

space form as

$$\begin{aligned}
L_{ae}(y, t) = & -\pi\rho_\infty b^2 \left[\ddot{w}_0 + U_n \dot{w}'_0 \tan \Lambda - U_n \dot{\phi} \right] - C_{L\phi} \rho_\infty U_n b \left[\dot{w}_0 - U_n \phi \right. \\
& \left. + U_n w'_0 \tan \Lambda - \frac{b}{2} \left(\frac{C_{L\phi}}{\pi} - 1 \right) \left(\dot{\phi} + U_n \phi' \tan \Lambda \right) - 0.165B_1 - 0.335B_2 \right], \tag{5a}
\end{aligned}$$

$$\begin{aligned}
T_{ae}(y, t) = & -\pi\rho_\infty b^3 \left\{ \left[\frac{1}{2} \left(\frac{C_{L\phi}}{\pi} - 1 \right) \left(U_n \dot{\phi} + U_n^2 \phi' \tan \Lambda \right) \right] \right. \\
& \left. + \frac{1}{8} b \left[\ddot{\phi} + U_n \dot{\phi}' \tan \Lambda \right] \right\} - \frac{1}{2} C_{L\phi} \rho_\infty U_n b^2 \left\{ \dot{w}_0 - U_n \phi + U_n w'_0 \tan \Lambda \right. \\
& \left. - \frac{b}{2} \left(\frac{C_{L\phi}}{\pi} - 1 \right) \left(\dot{\phi} + U_n \phi' \tan \Lambda \right) - 0.165B_1 - 0.335B_2 \right\}, \tag{5b}
\end{aligned}$$

where the local lift curve slope $C_{L\phi}$ is defined as

$$C_{L\phi} = \frac{L}{L + 2b \cos \Lambda} 2\pi, \tag{6}$$

and $B_i (i = 1, 2)$ satisfies the condition

$$\dot{B}_i(y, t) + \left(\frac{U_n}{b} \beta_i \right) B_i(y, t) = \dot{w}_{3c/4}(y, t), \quad (\beta_1 = 0.0455, \beta_2 = 0.3). \tag{7}$$

2.3. Aeroelastic governing equations and boundary conditions

The aeroelastic governing equations and the associated boundary conditions are derived from Hamilton's principle,

$$\delta J = \int_{t_1}^{t_2} [\delta T - \delta V + \delta W_e] dt = 0, \tag{8}$$

where t_1 and t_2 denote two arbitrary motions of time; T and V are the structural kinetic energy and the strain energy [22]; the virtual work due to unsteady aerodynamic loads W_e are defined as

$$W_e = \int_0^L [L_{ae} \delta w_0 + T_{ae} \delta \phi] dy. \tag{9}$$

In order to study the aeroelastic problems featuring bending-twist elastic coupling that is beneficial for the aeroelastic response behavior [13, 20, 32], the

host structure configured by the circumferentially asymmetric stiffness (CAS) [8, 33] lay-up is considered. As demonstrated in Refs. [4, 34], the elastic coupling of this type of beams can be split into two independent groups, viz., flapwise bending-twist-flapwise transverse shear and chordwise bending-extension-chordwise transverse shear elastic couplings. When the piezo-composite layers embedded in the biconvex cross-section beams is configured by CAS lay-up, the relation between piezoelectrically induced actuations and applied voltages can be simplified as

$$\begin{Bmatrix} \tilde{M}_x(y, t) \\ \tilde{M}_y(y, t) \\ \tilde{Q}_z(y, t) \\ \tilde{B}_w(y, t) \end{Bmatrix} = \begin{Bmatrix} \mathcal{A}_1^{Mx} & 0 \\ \mathcal{A}_1^{My} & 0 \\ 0 & \mathcal{A}_2^{Qz} \\ 0 & \mathcal{A}_2^{Bw} \end{Bmatrix} \begin{Bmatrix} V_1(t) \\ V_2(t) \end{Bmatrix} R(y), \quad (10)$$

where \tilde{M}_x , \tilde{M}_y , \tilde{Q}_z and \tilde{B}_w denote piezoelectrically induced bending moment (vertical), torque, flapwise transverse shear force and bimoment, respectively. Definitions of the associated piezo-coefficients \mathcal{A}_1^{Mx} , \mathcal{A}_1^{My} , \mathcal{A}_2^{Qz} and \mathcal{A}_2^{Bw} are given in the appendix of Ref. [22]. $R(y)$ denotes the piezo-actuator location along span

$$R(y) = H(y - y_{(k1)}) - H(y - y_{(k2)}), \quad (11)$$

where $H(\cdot)$ denotes Heaviside's distribution. The voltage parameters V_1 and V_2 are defined as

$$V_1(t) = \frac{1}{2} [V_T(t) - V_B(t)], \quad V_2(t) = \frac{1}{2} [V_T(t) + V_B(t)], \quad (12)$$

where V_T and V_B denote the voltages on the piezo-actuators located on the top and bottom of the wall, see Fig. 2.

Thus after a lengthy variation process of Eq. (8) and collecting the terms associated with the same variations (δw_0 , $\delta\phi$ and $\delta\theta_x$), the governing equations of the bending-twist subsystem that are of interest for the present problem are

$$\delta w_0 : a_{55}(w_0'' + \theta_x') + a_{56}\phi''' - b_1\ddot{w}_0 + L_{ae} + \delta_p \mathcal{A}_2^{Qz} V_2 R'(y) = 0, \quad (13a)$$

$$\begin{aligned} \delta\phi : a_{37}\theta''_x + a_{77}\phi'' - a_{66}\phi^{(iv)} - a_{56}(w_0''' + \theta''_x) - (b_4 + b_5)\ddot{\phi} \\ + (b_{10} + b_{18})\ddot{\phi}'' + T_{ae} + \delta_p \mathcal{A}_1^{My} V_1 R'(y) = 0, \end{aligned} \quad (13b)$$

$$\begin{aligned} \delta\theta_x : a_{33}\theta''_x + a_{37}\phi'' - a_{55}(w'_0 + \theta_x) - a_{56}\phi'' - (b_4 + b_{14})\ddot{\theta}_x \\ + \delta_p \mathcal{A}_1^{Mx} V_1 R'(y) - (\delta_p + \delta_s) \mathcal{A}_2^{Qz} V_2 R(y) = 0; \end{aligned} \quad (13c)$$

the boundary conditions are

at $y = 0$:

$$w_0 = \phi = \phi' = \theta_x = 0; \quad (14)$$

and at $y = L$:

$$\delta w_0 : a_{55}(w'_0 + \theta_x) + a_{56}\phi'' + \delta_s \mathcal{A}_2^{Qz} V_2 = 0, \quad (15a)$$

$$\delta\phi : a_{37}\theta'_x + a_{77}\phi' - a_{66}\phi''' - a_{56}(w_0'' + \theta'_x) + (b_{10} + b_{18})\ddot{\phi}'' + \delta_s \mathcal{A}_1^{My} V_1 = 0, \quad (15b)$$

$$\delta\phi' : -a_{56}(w'_0 + \theta_x) - a_{66}\phi'' = 0, \quad (15c)$$

$$\delta\theta_x : a_{33}\theta'_x + a_{37}\phi' + \delta_s \mathcal{A}_1^{Mx} V_1 = 0; \quad (15d)$$

where the stiffness coefficients a_{ij} and the inertial coefficients b_{ij} are defined in the appendix of Ref. [27]. Note that the traces are $\delta_p = 0$ and $\delta_s = 1$ for the case the actuator is spread over the entire beam span, otherwise their values are assumed as $\delta_p = 1$ and $\delta_s = 0$. In fact, the effect of the piezoelectrically induced flapwise transverse shear force \tilde{Q}_z on control authority is immaterial [22]. In addition, it can be strictly proved that $\mathcal{A}_2^{Qz} = 0$ for the case the piezo-composite layer are located symmetrically about z -axis as shown in Fig. 2. Therefore, the aeroelastic system described by Eqs. (13)-(15) is controlled solely by the voltage parameter V_1 .

2.4. State-space solution

Due to the high complexity arising from the elastic couplings and the boundary conditions, the spatial discretization via the extended Galerkin's method [35, 36] is implemented to cast the governing equations in state-space form. Thus the following spatial semi-discretization is introduced

$$w_0(y, t) = \mathbf{\Psi}_w^T(y) \mathbf{\Theta}_w \xi_s(t), \quad \phi(y, t) = \mathbf{\Psi}_\phi^T(y) \mathbf{\Theta}_\phi \xi_s(t),$$

$$\theta_x(y, t) = \mathbf{\Psi}_x^T(y) \mathbf{\Theta}_x \xi_s(t), \quad (16)$$

where the $1 \times N$ shape functions $\mathbf{\Psi}_w^T(y)$, $\mathbf{\Psi}_\phi^T(y)$ and $\mathbf{\Psi}_x^T(y)$ are required to fulfill only the geometric boundary conditions; $\mathbf{\Theta}_w$, $\mathbf{\Theta}_\phi$ and $\mathbf{\Theta}_x$ are $N \times m$ matrices consisting of the first m eigenmodes; ξ_s are the modal coordinates (e.g., see [37, p. 199]). Thus the state-space form of the aeroelastic governing equations are obtained as

$$\begin{Bmatrix} \dot{\mathbf{x}}_s \\ \dot{\mathbf{x}}_a \end{Bmatrix} = \begin{bmatrix} \mathbf{A}_s & \mathbf{B}_s \\ \mathbf{B}_a \mathbf{A}_s & \mathbf{A}_a + \mathbf{B}_a \mathbf{B}_s \end{bmatrix} \begin{Bmatrix} \mathbf{x}_s \\ \mathbf{x}_a \end{Bmatrix} + \begin{Bmatrix} \mathbf{0}_{m \times m} \\ \mathbf{M}^{-1} \\ \mathbf{D}_2 \mathbf{M}^{-1} \\ \mathbf{D}_2 \mathbf{M}^{-1} \end{Bmatrix} [\mathcal{A}V_1(t)] \quad (17)$$

In Eq. (17), \mathbf{x}_s and \mathbf{x}_a are $2m \times 1$ vectors that describe the motion of the blade and unsteady aerodynamic loads on the blade, respectively. The details of the matrices in Eq. (17) are given in Appendix A.

2.5. Velocity feedback control

In order to achieve the targets of vibration reduction and the expansion of the flight envelope, active control should be applied, making bending or twist velocities equal to zero ($\dot{\theta}_x = \dot{\phi} = 0$) as fast as possible. The classical negative velocity feedback control seems to be the straightforward and efficient choice for the control system design. The voltage parameter V_1 that governs the TB-subsystem can be given as [22]

$$V_1(t) = k_1[\alpha_1^k \dot{\phi}(Y_s, t) + \beta_1^k \dot{\theta}_x(Y_s, t)], \quad (18)$$

where k_1 is the control gain; α_1^k and β_1^k are the weighting coefficients on twist and bending velocities, respectively; Y_s is span location of the sensor offering the velocity information. Unless otherwise stated, the sensor is assumed at the wing tip, i.e., $Y_s = L$. Generally, the combined twist and velocity feedback control (for $\alpha_1^k \neq 0$ & $\beta_1^k \neq 0$ case) is the optimal control strategy. Whereas it is a difficult task to precisely determine the weighing coefficients for the global optimal control. For simplification, the individual twist or bending velocity feedback control is adopted here, i.e., $\alpha_1^k = 0$, $\beta_1^k = 1$ for Bending Control Methodology

$$V_1(t) = k_B \dot{\theta}_x(Y_s, t) = k_B \Psi_x^T(Y_s) \Theta_x \dot{\xi}_s(t), \quad (19)$$

and $\alpha_1^k = 1$, $\beta_1^k = 0$ for Twist Control Methodology

$$V_1(t) = k_T \dot{\phi}(Y_s, t) = k_T \Psi_\phi^T(Y_s) \Theta_\phi \dot{\xi}_s(t), \quad (20)$$

where k_B and k_T are the associated control gains. Thus the closed-loop system Eq. (17) becomes

$$\begin{Bmatrix} \dot{\mathbf{x}}_s \\ \dot{\mathbf{x}}_a \end{Bmatrix} = \begin{bmatrix} \hat{\mathbf{A}}_s & \mathbf{B}_s \\ \mathbf{B}_a \hat{\mathbf{A}}_s & \mathbf{A}_a + \mathbf{B}_a \mathbf{B}_s \end{bmatrix} \begin{Bmatrix} \mathbf{x}_s \\ \mathbf{x}_a \end{Bmatrix}, \quad (21)$$

where the expression of the modified matrix $\hat{\mathbf{A}}_s$ is given in Appendix A.

3. Numerical study

3.1. Validation

In order to validate our aeroelastic model, the wing structure model in Ref. [20] is used for validation. The material properties and geometric specification of the wing structure are shown in Table 1. The CAS lay-up configuration is given in Table 2. The actuating performance of piezo-composite materials has been validated in Ref. [22]. As for the pure aeroelastic model (without piezo-actuator embedded) present here, in fact, it is exactly the same as the one developed in Ref. [12]. Thus the main objective of this section is for code verification.

Table 1: Material property and geometric specification of the thin-walled beam with a biconvex cross-section [20]

Material	Value	Geometric	Value
E_{11}	$206.8 \times 10^9 \text{ N} \cdot \text{m}^{-2}$	Width ($2b^a$)	0.757 m
$E_{22} = E_{33}$	$5.17 \times 10^9 \text{ N} \cdot \text{m}^{-2}$	Depth ($2d^a$)	0.100 m
$G_{13} = G_{23}$	$2.55 \times 10^9 \text{ N} \cdot \text{m}^{-2}$	Wall thickness (h)	0.03 m
G_{12}	$3.10 \times 10^9 \text{ N} \cdot \text{m}^{-2}$	Number of layers (m_h)	6
$\mu_{12} = \mu_{13} = \mu_{23}$	0.25	Aspect ratio	16
ρ	$1528 \text{ Kg} \cdot \text{m}^{-3}$	Length (L)	6.058 m

^a The length is measured on the mid-line contour.

Table 2: CAS lay-up configurations for the thin-walled beam^a of Fig. 1 (deg).

Host structure	Top	Bottom	Piezo-actuator	Top	Bottom
Graphite-Epoxy	$[\theta_h]_6$	$[\theta_h]_6$	MFC	$[\theta_p]$	$[\theta_p]$

^a The piezo-actuator is positioned of the outer side of the laminate.

In the numerical study of the aeroelastic system, as a rule, high frequency modes of the wing structure that have negligible influences on the responses are normally ignored [11, 21]. Whereas, the explicit definition of "high frequency" should be identified. In other words, adequate structure modes should be taken into account for the balance of the precise description of the system and the computing scale. Fig. 3 depicts damping ratios induced by aerodynamics for selected number of structure modes when considering two typical freestream speeds near the onset of the flutter. It can be found that, at least, the first six modes should be accounted to ensure the accuracy of the calculation. Thus, unless other stated, the first six structure modes are adopted in the numerical study of the aeroelastic system.

Figures 4 and 5 plot the first five frequencies and the associated damping ratios as functions of freestream speed U_∞ , respectively. It can be seen that the lowest flutter speed in Fig. 5 and the eigen-frequencies near the onset of

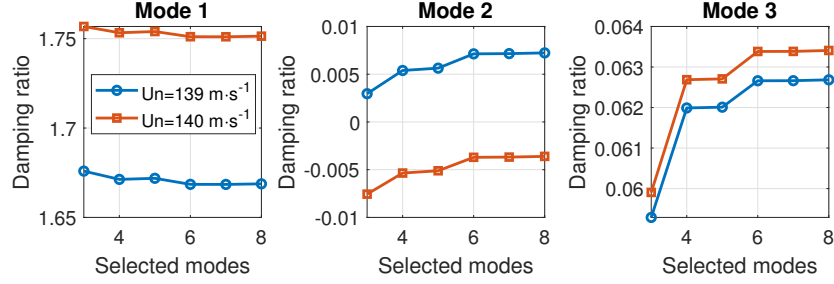


Figure 3: Aerodynamic damping ratios vs. selected first N th ($N = 3, 4, 5, 6, 7, 8$) structure modes.

flutter in Fig. 4 predicted by our approach all show excellent agreements with those in Ref. [20].

Figure 6 further highlights the influence of elastic tailoring on instability boundaries for selected swept wings. When in the domain $0^\circ < \theta_h < 90^\circ$, host structure ply-angle θ_h produces a negative elastic bending-twist coupling, leading to a very low divergence speed (indicated by $-o-$ lines), especially for forward-swept wings. However, when in the domain $95^\circ < \theta_h < 125^\circ$, the strong positive elastic bending-twist coupling leads to a higher divergence speed. Instead, flutter speed (indicated by $- \times -$ lines) becomes the lowest instability speed.

3.2. Piezo-coefficients study

The lay-up configuration and material properties of the piezo-actuator are presented in Tables 2 and 3, respectively. Three typical piezo-actuator circumference location configurations are accounted as shown Fig. 7, in capacity to present all cases for CAS lay-up configurations. Fig. 7 further shows the associated piezo-coefficients as a function of piezo-actuator ply-angle θ_p for the three cases. It can be found that piezoelectric flapwise transverse shear coefficient \mathcal{A}_2^{Qz} plotted in dashed line is negligible compared to that of piezoelectric chordwise transverse shear coefficient \mathcal{A}_2^{Qx} for Case 1. Furthermore, \mathcal{A}_2^{Qz} equals to zero for Case 2 and Case 3. Piezoelectric twist coefficient \mathcal{A}_1^{My} is proportional to the size of piezo-actuator. While piezoelectric flapwise bending \mathcal{A}_1^{Mx} of Case

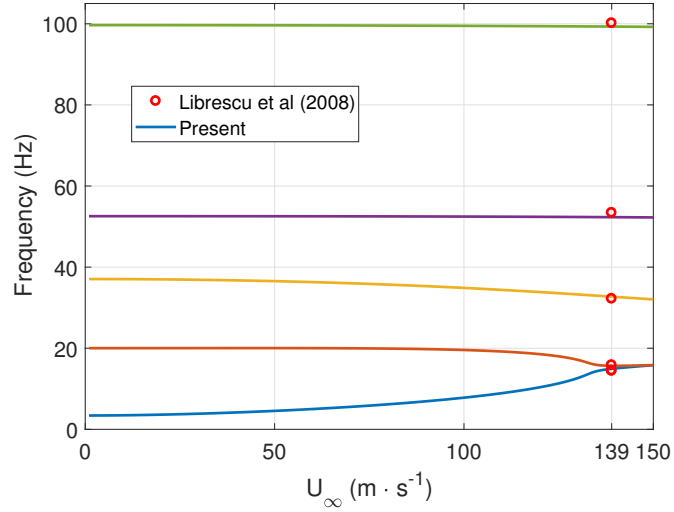


Figure 4: Frequency vs. freestream speed U_∞ ; $\theta_h = 105^\circ$, $\Lambda = 0^\circ$.

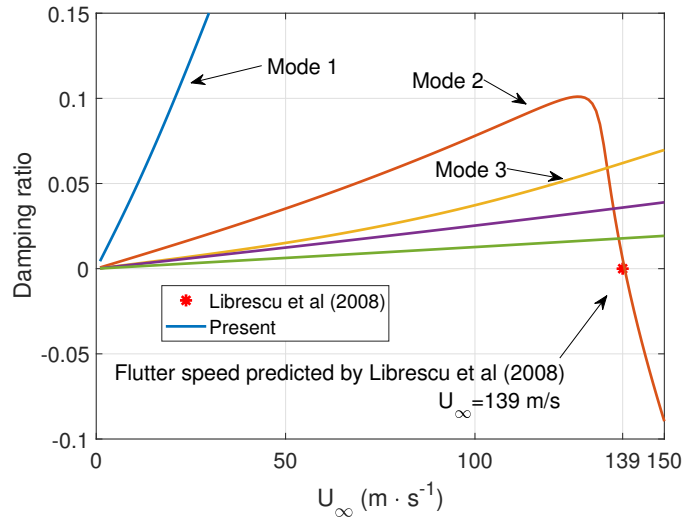


Figure 5: Damping ratio vs. freestream speed U_∞ ; $\theta_h = 105^\circ$, $\Lambda = 0^\circ$.

2 is greater than that of Case 1, since the average vertical distance between the top and bottom piezo-composite layers in Case 2 is longer than that in Case 1. Conclusively, in order to obtain maximum piezoelectrically induced actua-

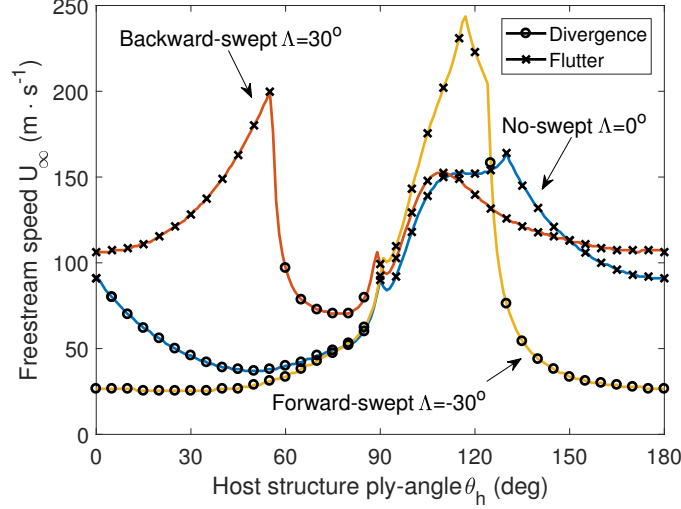


Figure 6: Flutter and divergence velocities vs. host structure ply-angle θ_h .

tions, the piezo-actuator covered over the entire cross-section as shown in Case 3 should be adopted.

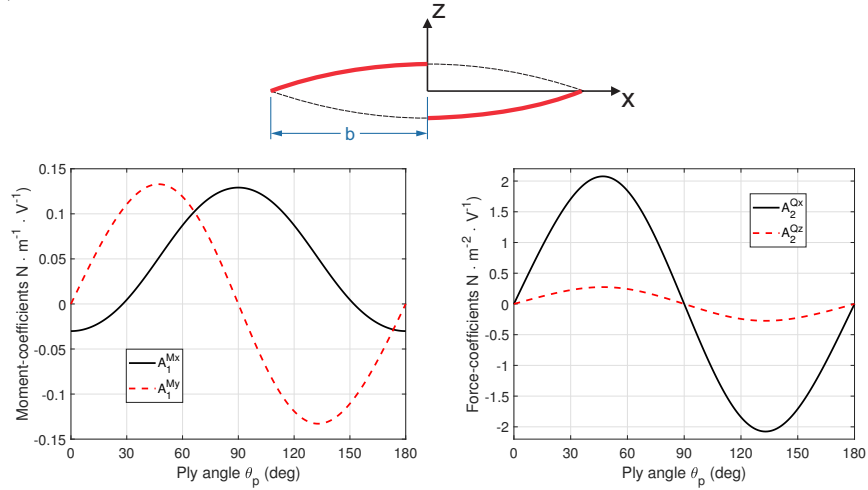
Table 3: Material properties of piezo-actuator [38, 39]

E_{11}	$31.28 \times 10^9 \text{ N} \cdot \text{m}^{-2}$	d_{11}	$386.63 \times 10^{-12} \text{ m} \cdot \text{V}^{-1}$
$E_{22} = E_{33}^*$	$17.05 \times 10^9 \text{ N} \cdot \text{m}^{-2}$	$d_{12} = d_{13}^*$	$-175.50 \times 10^{-12} \text{ m} \cdot \text{V}^{-1}$
$G_{12} = G_{13}^* = G_{23}^*$	$5.12 \times 10^9 \text{ N} \cdot \text{m}^{-2}$	ρ	$5115.9 \text{ Kg} \cdot \text{m}^{-3}$
$\mu_{12} = \mu_{13}^* = \mu_{23}^*$	0.303	m_p	1
Electrode spacing	0.4318 mm	Thickness	0.1905 mm

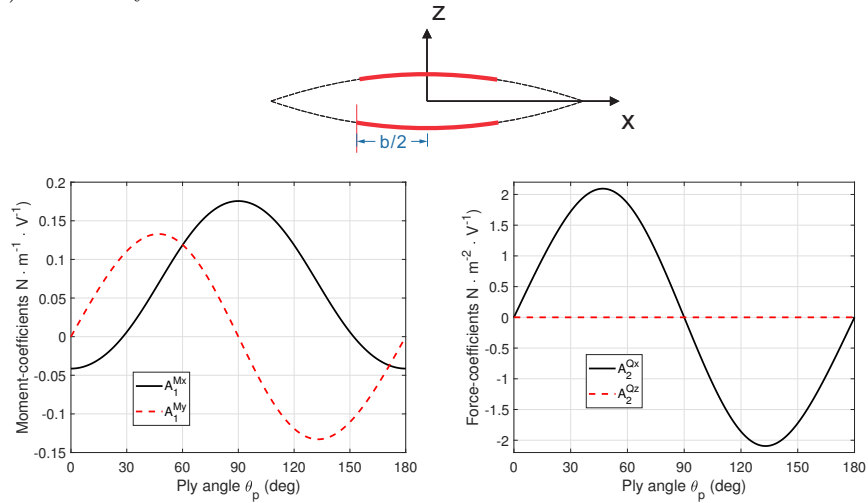
* The value is assumed by the author.

Adopted the configuration of Case 3, Fig. 8 plots the bending moment piezo-coefficient \mathcal{A}_1^{Mx} and torque piezo-coefficient \mathcal{A}_1^{My} as a function of piezo-actuator ply-angle θ_p for selected host structure cases. It can be seen that stiffness of the host structure has a significant effect on piezo-coefficients. In general, centered around $\theta_p = 90^\circ$, the curves of \mathcal{A}_1^{Mx} and \mathcal{A}_1^{My} exhibit a symmetric and an antisymmetric property, respectively. Furthermore, $\theta_p = 90^\circ$ yields

a) Case 1: antisymmetric about z -axis



b) Case 2: symmetric about z -axis



c) Case 3: fully covered

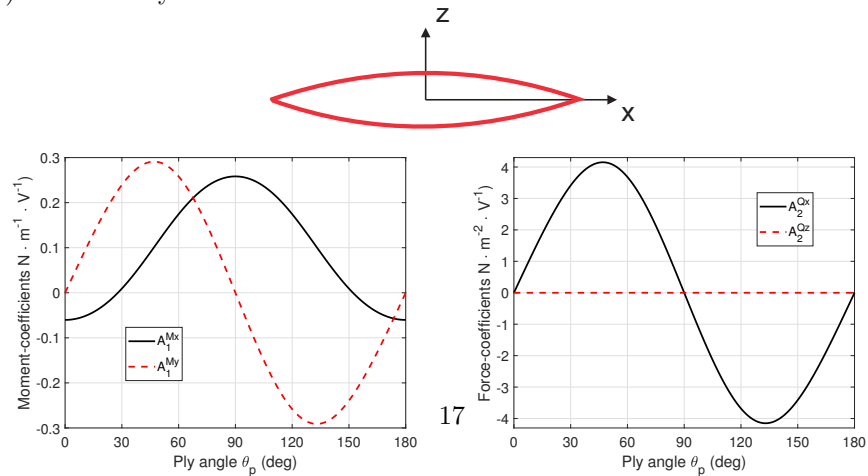


Figure 7: Piezo-coefficients vs. piezo-actuator ply-angle θ_p ; $\theta_h = 90^\circ$.

the maximum piezoelectric bending moment while the piezoelectric torque is immaterial.

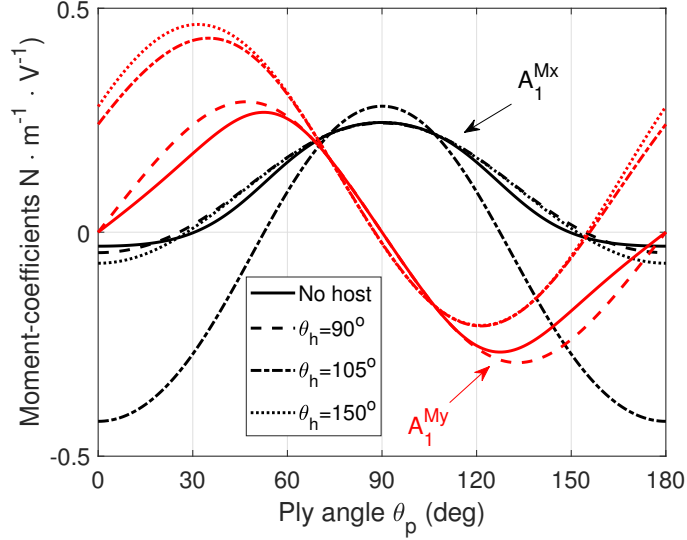


Figure 8: Piezo-coefficients vs. piezo-actuator ply-angle θ_p .

3.3. Damping ratio study for wing structure

We assume the piezo-actuator is distributed over the entire beam span. In order to focus on the wing structure, we assume the freestream speed $U_\infty = 0 \text{ m} \cdot \text{s}^{-1}$ in the aeroelastic system of Eq. (21). Recalling the instability boundaries in Fig. 6, two typical host structure cases are chosen for specific investigation, i.e., $\theta_h = 105^\circ$ characterizing strong bending-twist elastic coupling and $\theta_h = 150^\circ$ characterizing weaker elastic coupling.

For the excellent aeroleastic behavior [13] even for forward-swept wings, the structure with strong elastic coupling case $\theta_h = 105^\circ$ is investigated firstly. Fig. 9 depicts damping ratios of the first four modes as functions of piezo-actuator ply-angle θ_p . It can be found that no matter implementing the bending or the twist control methodology, the trends of all damping ratio curves show a similarity with that of torque piezo-coefficient \mathcal{A}_1^{My} in Fig. 8. This implies that

piezoelectric torque actuation plays a dominant role in the structure incorporating strong bending-twist elastic coupling. Based on the mode shape study, it can be identified that the bending motion is more significant than the twist motion in the first two modes, while the twist motion dominates the third mode. The result of Fig. 9 reveals that the twist control will even be more efficient than the direct bending control for bending motions. Note that for the third mode, bending control methodology produces a negative damping ratio while makes the first two modes exhibiting positive damping ratios. On the other hand, twist control methodology shows an extremely large positive damping ratio of the third mode when $\theta_p \approx 45^\circ$.

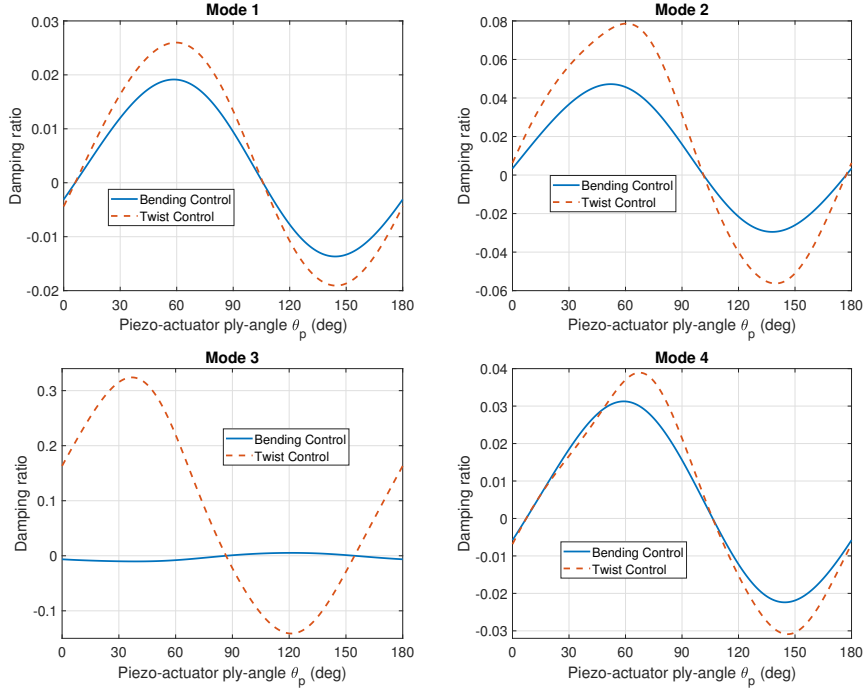


Figure 9: Damping ratios of the first four modes vs. piezo-actuator ply-angle θ_p ; $k_B = k_T = 400 \text{ V} \cdot \text{s}$, $\theta_h = 105^\circ$, $U_\infty = 0 \text{ m} \cdot \text{s}^{-1}$.

For the wing structure ($\theta_h = 150^\circ$) characterizing weak elastic coupling case, Fig. 10 compare damping ratios of the first four modes between twist and control methodologies. It can be found that depending on the mode shape dominated

by bending and twist component, bending and twist control methodologies have the significantly better control authority, respectively.

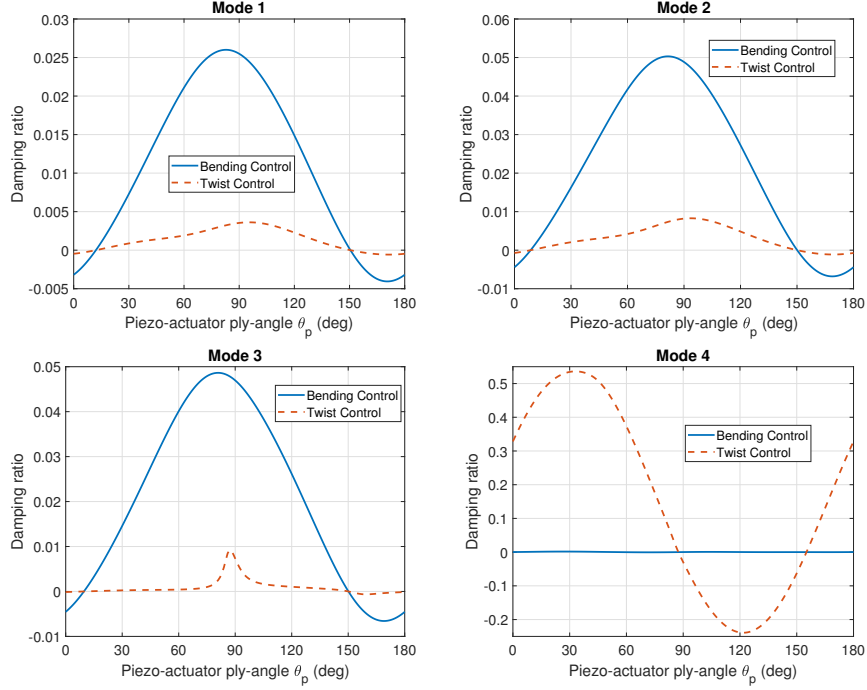


Figure 10: Damping ratios of the first four modes vs. piezo-actuator ply-angle θ_p ; $k_B = k_T = 400 \text{ V} \cdot \text{s}$, $\theta_h = 150^\circ$, $U_\infty = 0 \text{ m} \cdot \text{s}^{-1}$.

Control gain $k_T = k_B = 400 \text{ V} \cdot \text{s}$ is used in the previous damping ratios investigations. Fig. 11 presents the influence of control gains on control authority. In Fig. 11a, damping ratios linearly increase for $\theta_h = 150^\circ$ structure under the bending control strategy. Whereas, damping ratios of mode 2 and 3 begin to decrease slightly when control gain is greater than $500 \text{ V} \cdot \text{s}$ for $\theta_h = 105^\circ$ structure applied the twist control strategy, as shown in Fig. 11b.

3.4. Damping ratio study for aeroelastic system

Figure 12 plots damping ratios of the first four modes as functions of piezo-actuator ply-angle θ_p for an unswept wing ($\Lambda = 0^\circ$) with strong elastic coupling ($\theta_h = 105^\circ$) at freestream speed $U_\infty = 50 \text{ m} \cdot \text{s}^{-1}$. There is no doubt twist

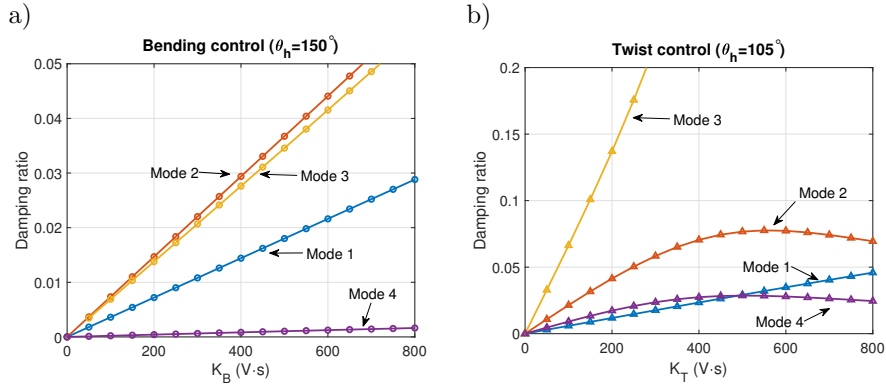


Figure 11: Damping ratios vs. control gain; $\theta_p = 45^\circ$; $U_\infty = 0 \text{ m} \cdot \text{s}^{-1}$.

control methodology has significantly better control performance. Actually, the aerodynamic load induced damping ratio (indicated by dotted lines) is large enough on the first mode in Fig. 12. Thus in order to improve the flight stability, more attention should be focused on the higher modes, especially the mode dominated by twist motion. Comparing damping ratio of mode 1 for the $U_\infty = 0 \text{ m} \cdot \text{s}^{-1}$ case in Fig. 9, piezo-actuator will induce negative damping ratios when $0^\circ < \theta_p < 30^\circ$ for the $U_\infty = 50 \text{ m} \cdot \text{s}^{-1}$ case in Fig. 12, implying aeroelastic effect has a considerable influence on control system performance. In summary, twist control with $\theta_p \approx 60^\circ$ can offer a balanced control performance for the first four modes.

Damping ratios of the aeroelastic system with weak bending-twist elastic coupling ($\theta_h = 150^\circ$) are reported in Fig. 13. In view of physical evidence that on the one hand aerodynamic lift and twist loads may enhance the coupling of twist-bending motion, on the other hand the aerodynamic load induced damping is already strong enough on bending motion, the twist control seems more essential than the bending control. Thus twist control with $\theta_p \approx 30^\circ$ is suggested for the aeroelastic system of $\theta_h = 150^\circ$.

3.5. Post-flutter study

One important target of active aeroelastic control is preventing or delaying the occurrence of flutter. Fig. 14 highlights the influence of additional piezo-

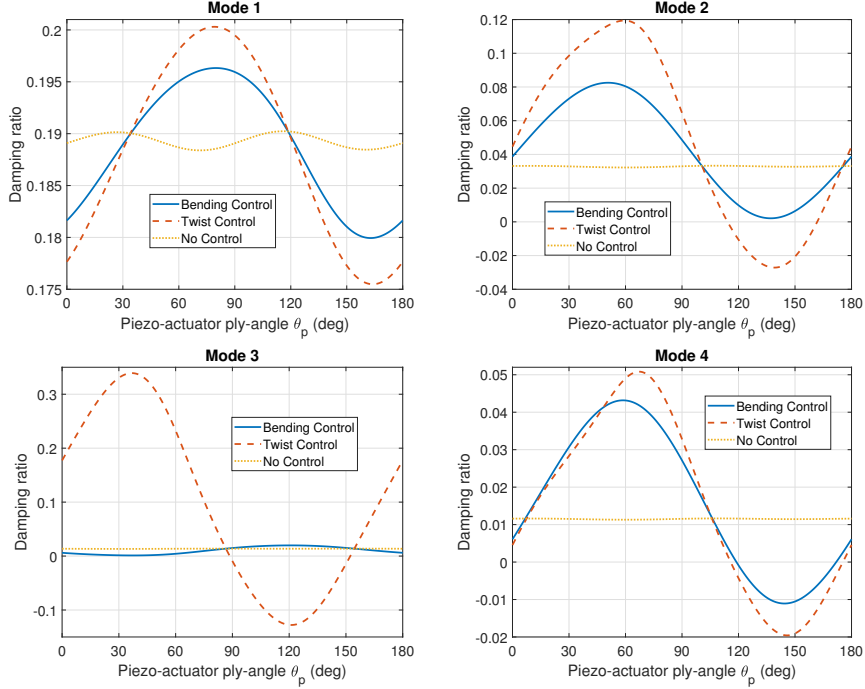


Figure 12: Damping ratio of the first four modes vs. piezo-actuator ply-angle θ_p ; $k_B = k_T = 400 \text{ V} \cdot \text{s}$, $\theta_h = 105^\circ$, $U_\infty = 50 \text{ m} \cdot \text{s}^{-1}$, $\Lambda = 0^\circ$.

composite layers on the lowest flutter speed. In Fig. 14, compared with the predicted flutter speed when ignoring the piezo-actuator plotted as solid lines, the additional mass and stiffness of piezo-composite layers have a non-ignorable effect on flutter speed, which are indicated by dashed lines. Specifically, ignoring the effect of mass and stiffness of the piezo-actuator in the modeling process may induce a maximum 10% error.

Firstly, an unswept wing ($\Lambda = 0^\circ$) with weak bending-twist elastic coupling ($\theta_h = 150^\circ$) is considered to study the active control near the onset of flutter. In Fig. 14, it can be found that the lowest flutter speed varies from $118 \text{ m} \cdot \text{s}^{-1}$ to $127 \text{ m} \cdot \text{s}^{-1}$ with the change of piezo-actuator ply-angle θ_p . Thus a freestream speed $U_\infty = 128 \text{ m} \cdot \text{s}^{-1}$ is applied to investigate the post-flutter control performance. Based on the associated eigenvalue and eigenvector study, it can be verified that the twist component dominates the unstable mode shape, viz., the

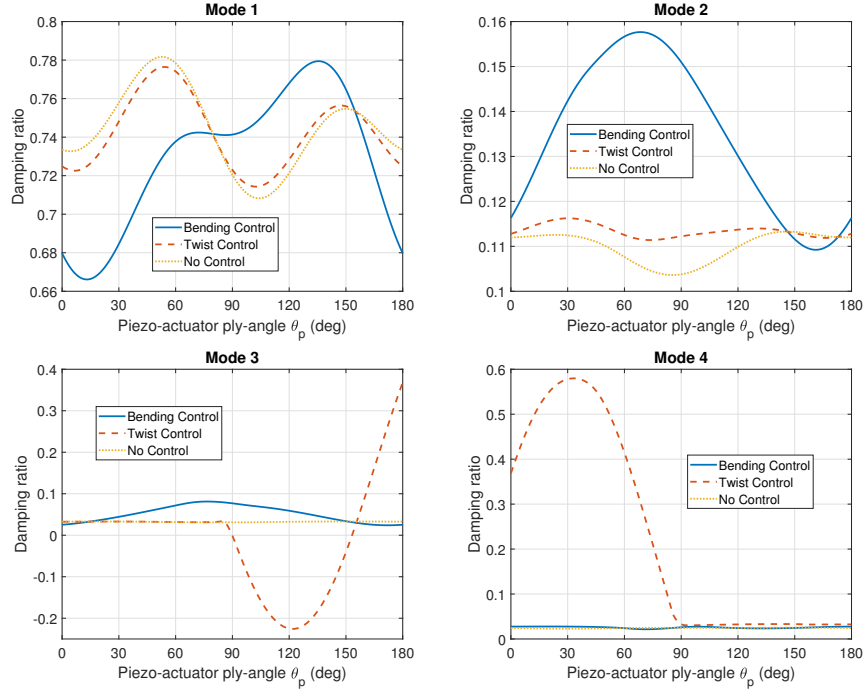


Figure 13: Damping ratio of the first mode vs. piezo-actuator ply-angle θ_p ; $k_B = k_T = 400 \text{ V} \cdot \text{s}$, $\theta_h = 150^\circ$, $U_\infty = 50 \text{ m} \cdot \text{s}^{-1}$, $\Lambda = 0^\circ$.

lowest flutter is dominated by the twist motion.

Figure 15 depicts damping ratio of the unstable mode as a function of piezo-actuator ply-angle θ_p for controlled and uncontrolled cases. Without control, the aerodynamic load will produce a negative damping ratio of the lowest twist mode which is indicated by the dotted line. When applying the twist control, the flutter mode will be stable when $0^\circ < \theta_p < 70^\circ$. On the contrary, bending control will make the flutter instability even worse.

In order to further investigate the influence of these two control methodologies on flutter speed, piezo-actuator with ply-angle $\theta_p = 30^\circ$ is selected to demonstrate the damping ratios near the onset of flutter in Fig. 16. Since the flutter mode is dominated by twist motion (in dotted line), bending control (in solid line) will decrease the lowest flutter speed. On the contrary, twist control (in dashed line) will improve the stability of the lowest twist mode and increase

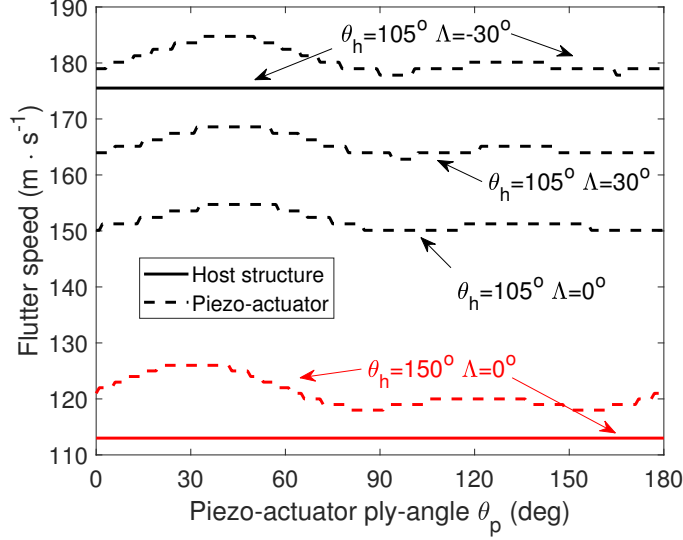


Figure 14: Lowest flutter speed vs. piezo-actuator ply-angle θ_p for selected host structure and sweep angle combinations.

the lowest flutter speed significantly. Note that, the lowest bending mode will become the flutter mode instead of the lowest twist mode when the aeroelastic system is under twist control.

Next, the aeroelastic system characterizing strong twist-bending elastic coupling ($\theta_h = 105^\circ$) is investigated. Figs. 17 and 18 show damping ratios of the unstable flutter mode of an unswept ($\Lambda = 0^\circ$) and a backward-swept ($\Lambda = 30^\circ$) wing cases, respectively. The results of Figs. 17 and 18 show that bending and twist control methodologies both lose control for preventing flutter, or even produce negative control effects near the onset of flutter. This is because, although the velocity feedback control improve the stability of mode 2, it makes mode 1 unstable even before the flutter speed. Therefore, at least, the information of twist and flapwise bending velocities should be both adopted for effective vibration suppression, in conjunction with a more comprehensive control strategy instead of the simple velocity feedback control.

However for the forward-swept wing ($\Lambda = -30^\circ$) case in Fig. 19, the simple

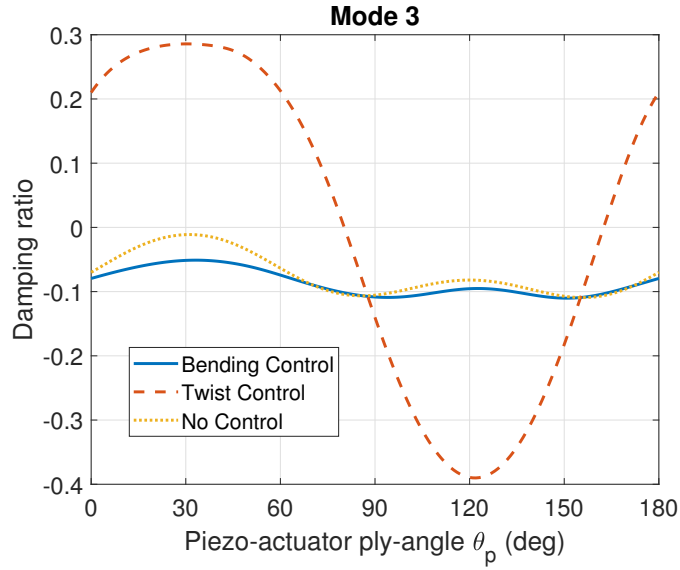


Figure 15: Damping ratio of the lowest twist mode vs. piezo-actuator ply-angle θ_p ; $k_B = k_T = 400 \text{ V} \cdot \text{s}$, $\theta_h = 150^\circ$, $\Lambda = 0^\circ$, $U_\infty = 128 \text{ m} \cdot \text{s}^{-1}$.

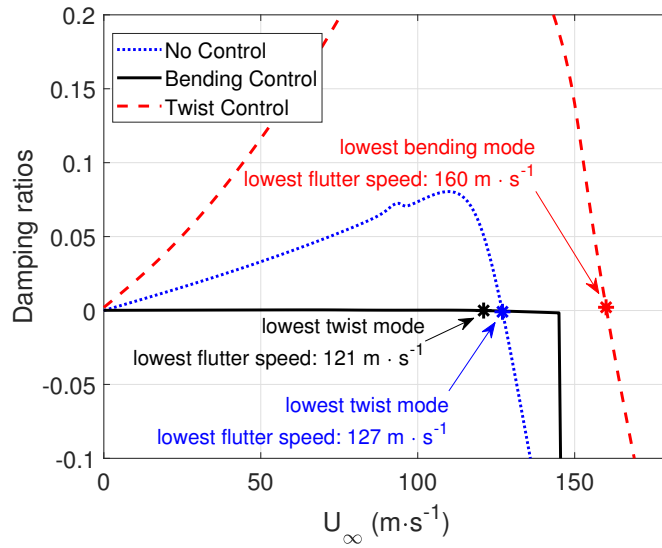


Figure 16: Damping ratio of the unstable flutter mode vs. freestream speed U_∞ ; $k_B = k_T = 400 \text{ V} \cdot \text{s}$, $\theta_h = 150^\circ$, $\theta_p = 30^\circ$, $\Lambda = 0^\circ$.

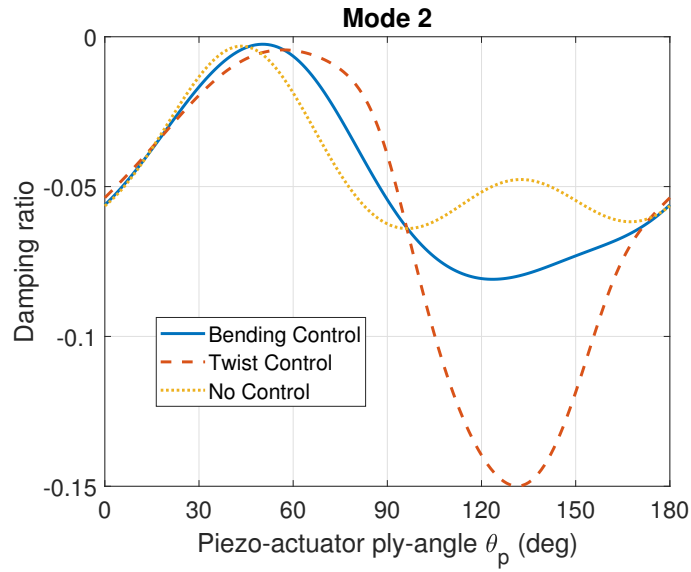


Figure 17: Damping ratio of the unstable flutter mode vs. piezo-actuator ply-angle θ_p ; $k_B = k_T = 400 \text{ V} \cdot \text{s}$, $\theta_h = 105^\circ$, $\Lambda = 0^\circ$, $U_\infty = 147 \text{ m} \cdot \text{s}^{-1}$.

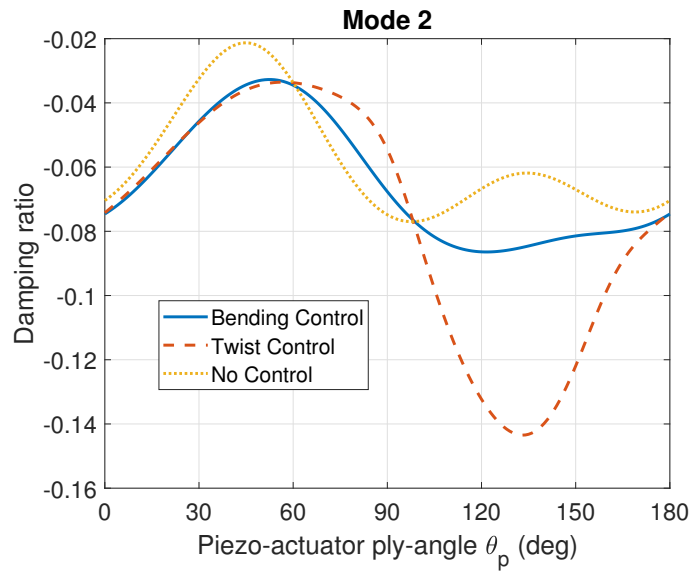


Figure 18: Damping ratio of the unstable flutter mode vs. piezo-actuator ply-angle θ_p ; $k_B = k_T = 400 \text{ V} \cdot \text{s}$, $\theta_h = 105^\circ$, $\Lambda = 30^\circ$, $U_\infty = 158 \text{ m} \cdot \text{s}^{-1}$.

velocity feedback control can keep mode 1 stable while improving the stability of mode 2 near the onset of flutter when piezo-actuator ply-angle around $\theta_p \approx 50^\circ$. This can be seen more clearly in the numerical simulations of the forward-swept

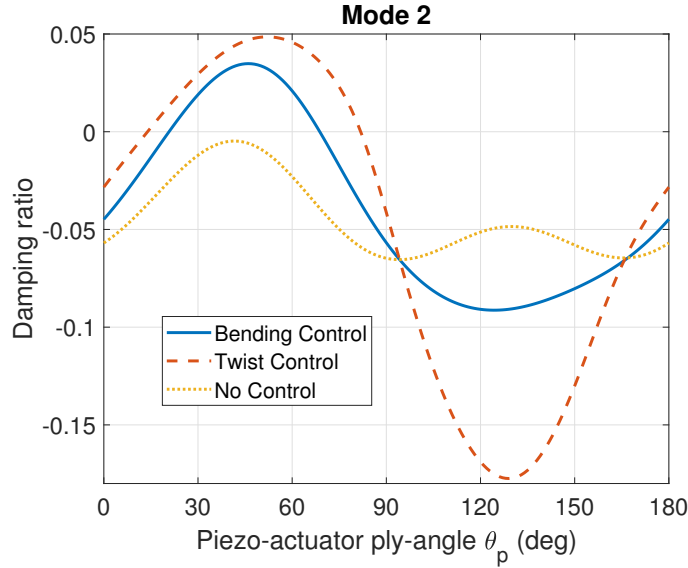


Figure 19: Damping ratio of the unstable mode vs. piezo-actuator ply-angle θ_p ; $k_B = k_T = 400 \text{ V} \cdot \text{s}$, $\theta_h = 105^\circ$, $\Lambda = -30^\circ$, $U_\infty = 186 \text{ m} \cdot \text{s}^{-1}$.

wing exposed to a sharp gust in Figs. 20 and 21. Figs. 20 and 21 display the tip bending and tip twist responses under a twist control for selected ply-angles θ_p , respectively. Fig. 22 further gives the associated voltage time-history applied on the piezo-actuator. Note that the results are simulated based on zero initial conditions. It can be found that twist control with $\theta_p = 50^\circ$ and $\theta_p = 45^\circ$ can both significantly prevent the occurrence of the flutter when the flight speed is slightly over the flutter speed. Whereas piezo-actuator with $\theta_p = 50^\circ$ can achieve the similar control authority as that of piezo-actuator with $\theta_p = 45^\circ$ does under a noticeably lower voltage.

Figure 23 plots flutter speeds as a function of twist control gain k_T for selected aircraft wing cases. The similar results can be obtained, i.e. twist control can improve the flutter speed significantly for weak elastic coupling

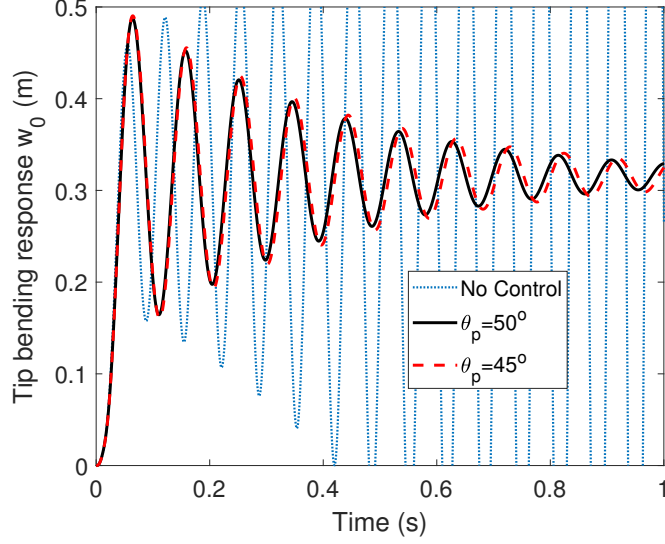


Figure 20: Tip bending response w_0 of a forward-swept wing subject to a sharp-edged gust near the onset of flutter under twist control methodology; $k_T = 400 \text{ V} \cdot \text{s}$, $\Lambda = -30^\circ$, $U_g = 10 \text{ m} \cdot \text{s}^{-1}$, $U_\infty = 187 \text{ m} \cdot \text{s}^{-1}$.

case, whereas this control strategy may make the situation even worse for the strong elastic coupling case.

4. Summary and conclusions

An efficient and comprehensive aeroelastic model based on a thin-walled beam theory incorporating fiber-reinforced and piezo-composite layers in incompressible flow has been proposed and formulated. Based on a velocity feedback control, the flight stability, especially on the occurrence of the flutter was demonstrated via the damping ratio study. The influence of sweep angle on control authority is also highlighted. Major conclusions are as follows.

1. The system is controlled by a coupling of piezoelectrically induced bending and twist when the piezo-actuators are circumferentially asymmetric stiffness (CAS) bonded or embedded in the host structure.

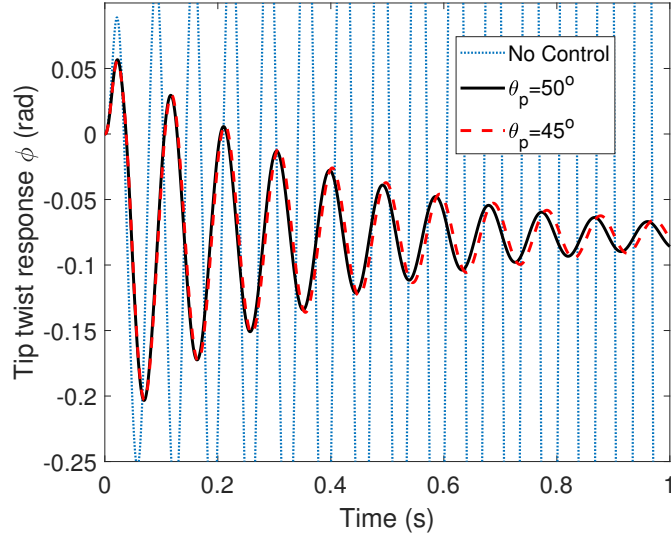


Figure 21: Tip twist response ϕ of a forward-swept wing subject to a sharp-edged gust near the onset of flutter under twist control methodology; $k_T = 400 \text{ V} \cdot \text{s}$, $\Lambda = -30^\circ$, $U_g = 10 \text{ m} \cdot \text{s}^{-1}$, $U_\infty = 187 \text{ m} \cdot \text{s}^{-1}$.

2. The stiffness of the anisotropic host structure has a significant effect on piezo-coefficients.
3. The simple twist velocity feedback control with the piezo-actuator consisting maximum piezoelectrically torque can improve the flutter speed significantly for the weak elastic coupling wing structure.
4. Whereas, for the strong elastic coupling wing structure, information of twist and flapwise bending velocities should be both adopted for effective vibration suppression, in conjunction with a more comprehensive control strategy instead of the simple velocity feedback control.
5. The control system should be carefully examined for all available flight envelope during the design stage, since aeroelastic effect has a considerable influence on control authority.

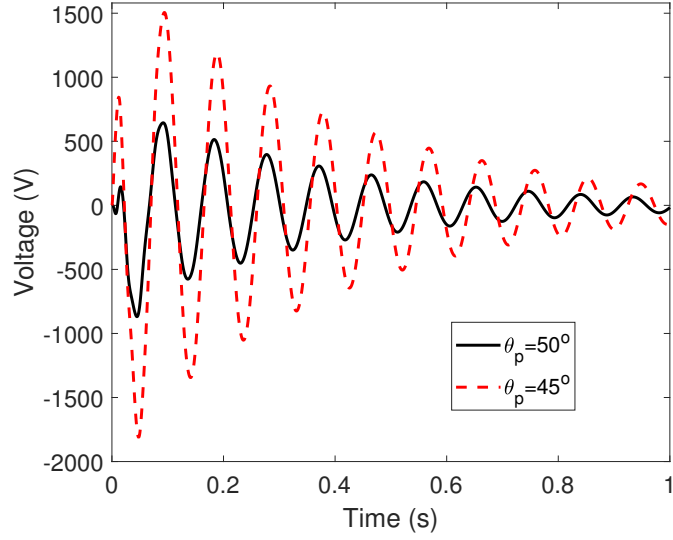


Figure 22: Voltage V_1 applied on the actuators of a forward-swept wing subject to a sharp-edged gust near the onset of flutter under twist control methodology; $k_T = 400 \text{ V} \cdot \text{s}$, $\Lambda = -30^\circ$, $U_g = 10 \text{ m} \cdot \text{s}^{-1}$, $U_\infty = 187 \text{ m} \cdot \text{s}^{-1}$.

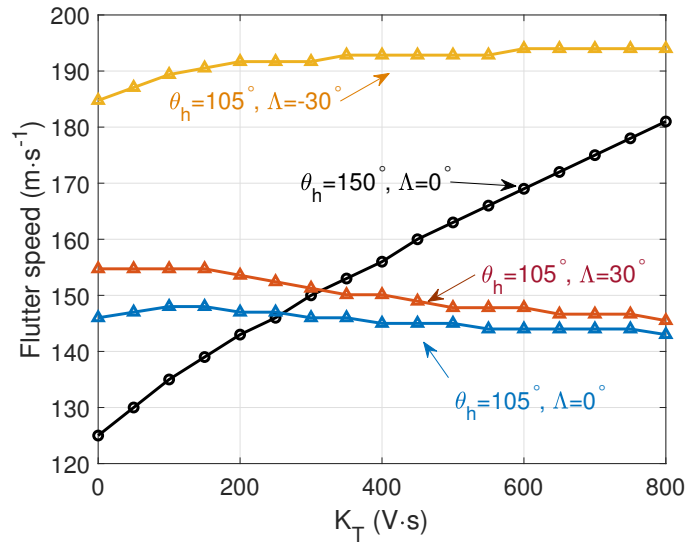


Figure 23: Flutter speed vs. twist control gain k_T ; $\theta_p = 45^\circ$.

5. Acknowledgments

The author Xiao Wang thanks Prof. Zhanming Qin for his helpful discussions and comments. The authors are indebted for the financial support of National Natural Science Foundation of China (No. 11802120).

Appendix A. Definition of matrices

$$[\mathbf{A}_s]_{2m \times 2m} = \begin{bmatrix} \mathbf{0}_{m \times m} & \mathbf{I}_{m \times m} \\ -\mathbf{M}^{-1}\mathbf{K} & -\mathbf{M}^{-1}\mathbf{C} \end{bmatrix}, \quad (\text{A.1})$$

$$[\mathbf{B}_s]_{2m \times 2m} = \begin{bmatrix} \mathbf{0}_{m \times 2m} \\ -(C_{L\phi}\rho_\infty b U_n)\mathbf{M}^{-1} \begin{bmatrix} \alpha_1 \mathbf{I}_{m \times m} & \alpha_2 \mathbf{I}_{m \times m} \end{bmatrix} \end{bmatrix}, \quad (\text{A.2})$$

$$[\mathbf{A}_a]_{2m \times 2m} = \begin{bmatrix} -\beta_1 \mathbf{I}_{m \times m} & \mathbf{0}_{m \times m} \\ \mathbf{0}_{m \times m} & -\beta_2 \mathbf{I}_{m \times m} \end{bmatrix}, \quad (\text{A.3})$$

$$[\mathbf{B}_a]_{2m \times 2m} = \begin{bmatrix} \mathbf{I}_{m \times m} \\ \mathbf{I}_{m \times m} \end{bmatrix} \begin{bmatrix} \mathbf{D}_1 & \mathbf{D}_2 \end{bmatrix}_{m \times 2m}, \quad (\text{A.4})$$

$$\begin{aligned} \mathbf{D}_1 = \int_0^L & \left(\boldsymbol{\Theta}_w^T \boldsymbol{\Psi}_w + \frac{1}{2} b \boldsymbol{\Theta}_\phi^T \boldsymbol{\Psi}_\phi \right) U_n \left[\boldsymbol{\Psi}'_w{}^T \boldsymbol{\Theta}_w \dot{\xi}_s \tan \Lambda - \boldsymbol{\Psi}'_\phi{}^T \boldsymbol{\Theta}_\phi \dot{\xi}_s \right. \\ & \left. - \frac{1}{2} b \boldsymbol{\Psi}'_\phi{}^T \boldsymbol{\Theta}_\phi \dot{\xi}_s \tan \Lambda \left(\frac{C_{L\phi}}{\pi} - 1 \right) \right] \mathrm{d}y, \end{aligned} \quad (\text{A.5})$$

$$\mathbf{D}_2 = \int_0^L \left(\boldsymbol{\Theta}_w^T \boldsymbol{\Psi}_w + \frac{1}{2} b \boldsymbol{\Theta}_\phi^T \boldsymbol{\Psi}_\phi \right) \left[\boldsymbol{\Psi}_w^T \boldsymbol{\Theta}_w \ddot{\xi}_s - \frac{1}{2} b \boldsymbol{\Psi}_\phi^T \boldsymbol{\Theta}_\phi \ddot{\xi}_s \left(\frac{C_{L\phi}}{\pi} - 1 \right) \right] \mathrm{d}y, \quad (\text{A.6})$$

$$\mathcal{A} = \int_0^L \left[\mathcal{A}_1^{My} \boldsymbol{\Theta}_\phi^T \boldsymbol{\Psi}_\phi + \mathcal{A}_1^{Mx} \boldsymbol{\Theta}_x^T \boldsymbol{\Psi}_x \right] R'(y) \mathrm{d}y. \quad (\text{A.7})$$

In the above equations, \mathbf{M} and \mathbf{K} are the mass and stiffness matrices of the wing structure; \mathbf{C} is the pneumatic damping matrix; \mathbf{Q}_g denotes the external gust loads; \mathcal{A} is the actuating matrix; \mathbf{D}_1 and \mathbf{D}_2 are related to Wagner's function.

$$[\hat{\mathbf{A}}_s]_{2m \times 2m} = \begin{bmatrix} \mathbf{0}_{m \times m} & \mathbf{I}_{m \times m} \\ -\mathbf{M}^{-1}\mathbf{K} & -\mathbf{M}^{-1}(\mathbf{C} + \mathbf{P}_{T/B}) \end{bmatrix}, \quad (\text{A.8})$$

where

$$\mathbf{P}_T = k_T \mathcal{A} \boldsymbol{\Psi}_x^T(Y_s) \boldsymbol{\Theta}_x, \quad (\text{A.9a})$$

$$\mathbf{P}_B = k_B \mathcal{A} \boldsymbol{\Psi}_\phi^T(Y_s) \boldsymbol{\Theta}_\phi. \quad (\text{A.9b})$$

References

- [1] E. Forster, S. Clay, R. Holzwarth, D. Paul, Flight vehicle composite structures, in: The 26th Congress of ICAS and 8th AIAA ATIO, 2008, p. 8976.
- [2] C. E. Harris, J. H. Starnes, M. J. Shuart, Design and manufacturing of aerospace composite structures, state-of-the-art assessment, *Journal of Aircraft* 39 (4) (2002) 545–560.
- [3] L. Librescu, S. Na, P. Marzocca, C. Chung, M. K. Kwak, Active aeroelastic control of 2-d wing-flap systems operating in an incompressible flowfield and impacted by a blast pulse, *Journal of Sound and Vibration* 283 (3) (2005) 685–706.
- [4] L. Librescu, O. Song, Behavior of thin-walled beams made of advanced composite materials and incorporating non-classical effects, *Appl. Mech. Rev.* 44 (11) (1991) S174–80.
- [5] L. W. Rehfield, A. R. Atilgan, D. H. Hodges, Nonclassical behavior of thin-walled composite beams with closed cross sections, *Journal of the American Helicopter Society* 35 (2) (1990) 42–50.
- [6] D. S. Dancila, E. A. Armanios, The influence of coupling on the free vibration of anisotropic thin-walled closed-section beams, *International Journal of Solids and Structures* 35 (23) (1998) 3105–3119.
- [7] R. Chandra, I. Chopra, Structural response of composite beams and blades with elastic couplings, *Composites Engineering* 2 (5-7) (1992) 347–374.
- [8] E. Smith, I. Chopra, Formulation and evaluation of an analytical model for composite box-beams, *J. Am. Helicopter Soc.* 36 (3) (1991) 23–35.
- [9] R. Chandra, I. Chopra, Experimental-theoretical investigation of the vibration characteristics of rotating composite box beams, *Journal of Aircraft* 29 (4) (1992) 657–664.

- [10] L. Librescu, O. Song, *Thin-Walled Composite Beams: Theory and Application*, Springer, New York, 2006, chap.8, pp. 213-232.
- [11] Z. Qin, L. Librescu, P. Marzocca, Aeroelasticity of composite aerovehicle wings in supersonic flows, *Journal of spacecraft and rockets* 40 (2) (2003) 162–173.
- [12] Z. Qin, L. Librescu, Dynamic aeroelastic response of aircraft wings modeled as anisotropic thin-walled beams, *Journal of Aircraft* 40 (3) (2003) 532–543.
- [13] L. Librescu, A. Khdeir, Aeroelastic divergence of swept-forward composite wings including warping restraint effect, *AIAA journal* 26 (11) (1988) 1373–1377.
- [14] G. Karpouzian, L. Librescu, Nonclassical effects on divergence and flutter of anisotropic swept aircraft wings, *AIAA journal* 34 (4) (1996) 786–794.
- [15] R. Chandra, A. D. Stemple, I. Chopra, Thin-walled composite beams under bending, torsional, and extensional loads, *Journal of Aircraft* 27 (7) (1990) 619–626.
- [16] C. Hwu, Z. Tsai, Aeroelastic divergence of stiffened composite multicell wing structures, *Journal of Aircraft* 39 (2) (2002) 242–251.
- [17] V. V. Volovoi, D. H. Hodges, Single-and multicelled composite thin-walled beams, *AIAA journal* 40 (5) (2002) 960–965.
- [18] L. Librescu, P. Marzocca, Advances in the linear/nonlinear control of aeroelastic structural systems, *Acta Mechanica* 178 (3-4) (2005) 147–186.
- [19] S. Na, L. Librescu, Oscillation control of cantilevers via smart materials technology and optimal feedback control: actuator location and power consumption issues, *Smart Materials and Structures* 7 (6) (1998) 833.
- [20] L. Librescu, S. Na, Z. Qin, B. Lee, Active aeroelastic control of aircraft composite wings impacted by explosive blasts, *J. Sound Vib.* 318 (1) (2008) 74–92.

- [21] S. Na, J.-S. Song, J.-H. Choo, Z. Qin, Dynamic aeroelastic response and active control of composite thin-walled beam structures in compressible flow, *Journal of Sound and Vibration* 330 (21) (2011) 4998–5013.
- [22] X. Wang, M. Morandini, P. Masarati, Velocity feedback damping of piezo-actuated wings, *Composite Structures* 174 (2017) 221–232.
- [23] X. Wang, M. Morandini, P. Masarati, Modeling and control for rotating pretwisted thin-walled beams with piezo-composite, *Composite Structures* 180 (2017) 647–663.
- [24] W. K. Wilkie, R. G. Bryant, J. W. High, R. L. Fox, R. F. Hellbaum, A. Jalink Jr, B. D. Little, P. H. Mirick, Low-cost piezocomposite actuator for structural control applications, in: *SPIE’s 7th Annual International Symposium on Smart Structures and Materials*, International Society for Optics and Photonics, 2000, pp. 323–334.
- [25] A. A. Bent, Active fiber composites for structural actuation, Ph.D. thesis, Massachusetts Institute of Technology (1997).
- [26] Z. Qin, L. Librescu, On a shear-deformable theory of anisotropic thin-walled beams: further contribution and validation, *Compos. Struct.* 56 (4) (2002) 345–358.
- [27] X. Wang, Z. Qin, Nonlinear modal interactions in composite thin-walled beam structures with simultaneous 1: 2 internal and 1: 1 external resonances, *Nonlinear Dynamics* 86 (2) (2016) 1381–1405.
- [28] W. P. RODDEN, B. STAHL, A strip method for prediction of damping in subsonic wind tunnel andflight flutter tests., *Journal of Aircraft* 6 (1) (1969) 9–17.
- [29] E. Carson, Calculation of flutter characteristics for finite-span.
- [30] T. V. Karman, Airfoil theory for non-uniform motion, *Journal of the Aeronautical Sciences* 5 (10) (1938) 379–390.

- [31] R. L. Bisplinghoff, H. Ashley, R. L. Halfman, *Aeroelasticity*, Courier Corporation, 2013.
- [32] L. Librescu, J. Simovich, General formulation for the aeroelastic divergence of composite swept-forward wing structures, *Journal of Aircraft* 25 (4) (1988) 364–371.
- [33] O. Song, L. Librescu, Free vibration of anisotropic composite thin-walled beams of closed cross-section contour., *J. Sound Vib.* 167 (1) (1993) 129–47.
- [34] L. Librescu, L. Meirovitch, O. Song, Refined structural modeling for enhancing vibrational and aeroelastic characteristics of composite aircraft wings, *Recherche Aerospaciale* (1) (1996) 23–35.
- [35] A. Palazotto, P. Linnemann, Vibration and buckling characteristics of composite cylindrical panels incorporating the effects of a higher order shear theory, *Int. J. Solids Struct.* 28 (3) (1991) 341–361.
- [36] L. Librescu, S. Na, Dynamic response of cantilevered thin-walled beams to blast and sonic-boom loadings, *Shock. Vib.* 5 (1) (1998) 23–33.
- [37] L. Meirovitch, *Principles and Techniques of Vibrations*, Prentice Hall, Upper Saddle River, New Jersey, 1997.
- [38] J.-S. Park, J.-H. Kim, Analytical development of single crystal macro fiber composite actuators for active twist rotor blades, *Smart Mater. Struct.* 14 (4) (2005) 745.
- [39] R. B. Williams, D. J. Inman, M. R. Schultz, M. W. Hyer, W. K. Wilkie, Nonlinear tensile and shear behavior of macro fiber composite actuators, *Journal of Composite Materials* 38 (10) (2004) 855–869.

List of Figures

1	Geometry of an aircraft wing modeled as thin-walled beam with a biconvex cross-section (local coordinate frame (s, y, n) is on the mid-line contour of the cross-section).	6
2	A smart aircraft wing with piezo-actuator.	6
3	Aerodynamic damping ratios vs. selected first N th ($N = 3, 4, 5, 6, 7, 8$) structure modes.	14
4	Frequency vs. freestream speed U_∞ ; $\theta_h = 105^\circ$, $\Lambda = 0^\circ$	15
5	Damping ratio vs. freestream speed U_∞ ; $\theta_h = 105^\circ$, $\Lambda = 0^\circ$	15
6	Flutter and divergence velocities vs. host structure ply-angle θ_h	16
7	Piezo-coefficients vs. piezo-actuator ply-angle θ_p ; $\theta_h = 90^\circ$	17
8	Piezo-coefficients vs. piezo-actuator ply-angle θ_p	18
9	Damping ratios of the first four modes vs. piezo-actuator ply-angle θ_p ; $k_B = k_T = 400 \text{ V} \cdot \text{s}$, $\theta_h = 105^\circ$, $U_\infty = 0 \text{ m} \cdot \text{s}^{-1}$	19
10	Damping ratios of the first four modes vs. piezo-actuator ply-angle θ_p ; $k_B = k_T = 400 \text{ V} \cdot \text{s}$, $\theta_h = 150^\circ$, $U_\infty = 0 \text{ m} \cdot \text{s}^{-1}$	20
11	Damping ratios vs. control gain; $\theta_p = 45^\circ$; $U_\infty = 0 \text{ m} \cdot \text{s}^{-1}$	21
12	Damping ratio of the first four modes vs. piezo-actuator ply-angle θ_p ; $k_B = k_T = 400 \text{ V} \cdot \text{s}$, $\theta_h = 105^\circ$, $U_\infty = 50 \text{ m} \cdot \text{s}^{-1}$, $\Lambda = 0^\circ$	22
13	Damping ratio of the first mode vs. piezo-actuator ply-angle θ_p ; $k_B = k_T = 400 \text{ V} \cdot \text{s}$, $\theta_h = 150^\circ$, $U_\infty = 50 \text{ m} \cdot \text{s}^{-1}$, $\Lambda = 0^\circ$	23
14	Lowest flutter speed vs. piezo-actuator ply-angle θ_p for selected host structure and sweep angle combinations.	24
15	Damping ratio of the lowest twist mode vs. piezo-actuator ply-angle θ_p ; $k_B = k_T = 400 \text{ V} \cdot \text{s}$, $\theta_h = 150^\circ$, $\Lambda = 0^\circ$, $U_\infty = 128 \text{ m} \cdot \text{s}^{-1}$	25
16	Damping ratio of the unstable flutter mode vs. freestream speed U_∞ ; $k_B = k_T = 400 \text{ V} \cdot \text{s}$, $\theta_h = 150^\circ$, $\theta_p = 30^\circ$, $\Lambda = 0^\circ$	25

17	Damping ratio of the unstable flutter mode vs. piezo-actuator ply-angle θ_p ; $k_B = k_T = 400 \text{ V} \cdot \text{s}$, $\theta_h = 105^\circ$, $\Lambda = 0^\circ$, $U_\infty = 147 \text{ m} \cdot \text{s}^{-1}$	26
18	Damping ratio of the unstable flutter mode vs. piezo-actuator ply-angle θ_p ; $k_B = k_T = 400 \text{ V} \cdot \text{s}$, $\theta_h = 105^\circ$, $\Lambda = 30^\circ$, $U_\infty = 158 \text{ m} \cdot \text{s}^{-1}$	26
19	Damping ratio of the unstable mode vs. piezo-actuator ply-angle θ_p ; $k_B = k_T = 400 \text{ V} \cdot \text{s}$, $\theta_h = 105^\circ$, $\Lambda = -30^\circ$, $U_\infty = 186 \text{ m} \cdot \text{s}^{-1}$	27
20	Tip bending response w_0 of a forward-swept wing subject to a sharp-edged gust near the onset of flutter under twist control methodology; $k_T = 400 \text{ V} \cdot \text{s}$, $\Lambda = -30^\circ$, $U_g = 10 \text{ m} \cdot \text{s}^{-1}$, $U_\infty = 187 \text{ m} \cdot \text{s}^{-1}$	28
21	Tip twist response ϕ of a forward-swept wing subject to a sharp-edged gust near the onset of flutter under twist control methodology; $k_T = 400 \text{ V} \cdot \text{s}$, $\Lambda = -30^\circ$, $U_g = 10 \text{ m} \cdot \text{s}^{-1}$, $U_\infty = 187 \text{ m} \cdot \text{s}^{-1}$	29
22	Voltage V_1 applied on the actuators of a forward-swept wing subject to a sharp-edged gust near the onset of flutter under twist control methodology; $k_T = 400 \text{ V} \cdot \text{s}$, $\Lambda = -30^\circ$, $U_g = 10 \text{ m} \cdot \text{s}^{-1}$, $U_\infty = 187 \text{ m} \cdot \text{s}^{-1}$	30
23	Flutter speed vs. twist control gain k_T ; $\theta_p = 45^\circ$	30

List of Tables

1	Material property and geometric specification of the thin-walled beam with a biconvex cross-section [20]	13
2	CAS lay-up configurations for the thin-walled beam ^a of Fig. 1 (deg).	13
3	Material properties of piezo-actuator [38, 39]	16